Supplement for "Ice growth driven by the Wegener-Bergeron-Findeisen process in expansion chamber simulations: roles of ascent rate and particle sedimentation"

Inyeob La[1], Wojciech W. Grabowski[2,3], Shin-ichiro Shima[1,4], and Seong Soo Yum[5,6]
[1]Graduate School of Information Science, University of Hyogo, Kobe, Japan
[2]MMM Laboratory, NSF National Center for Atmospheric Research, Boulder, CO, USA
[3]Institute of Geophysics, Faculty of Physics, University of Warsaw, Warsaw, Poland
[4]RIKEN Center for Computational Science, Kobe, Japan
[5]Climate and Environmental Research Institute, Korea Institute of Science and Technology, Seoul, Republic of Korea
[6]Department of Atmospheric Sciences, Yonsei University, Seoul, Republic of Korea

Correspondence to: Inyeob La (inyeob.la@gsis.u-hyogo.ac.jp) and Seong Soo Yum (ssyum@kist.re.kr)

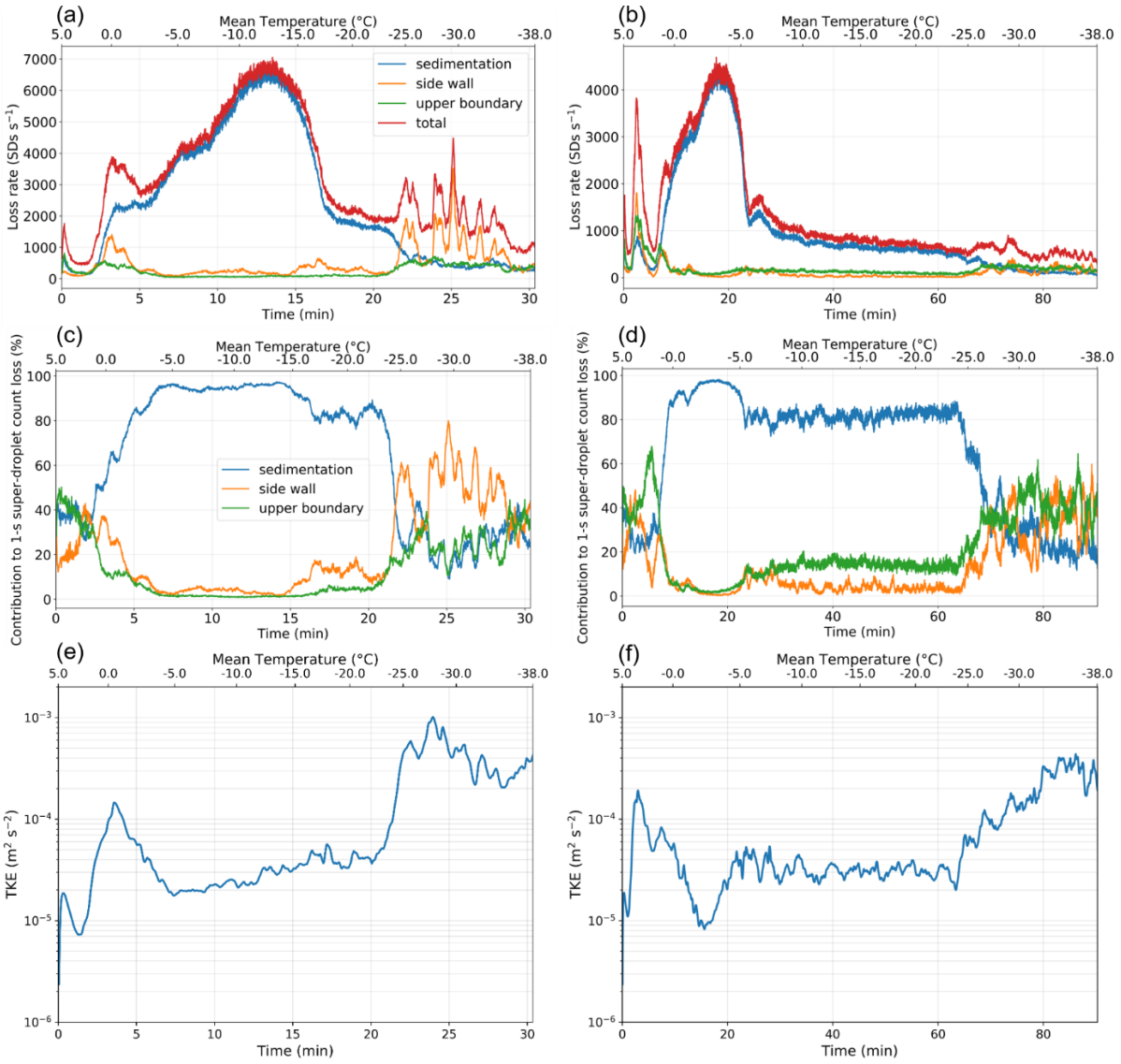


Figure S1. Removal-pathway diagnostic for polluted EVAP simulations with gravity. The left column shows the reference case with w = 3 m s^{-1}, and the right column shows the slower-ascent case with w = 1 m s^{-1}. Panels (a,b) show super-droplet count loss rates through lower-boundary sedimentation, side-wall loss, and upper-boundary loss, computed from 1-s increments of the cumulative removal counters. The red line shows the total loss rate. Panels (c,d) show the relative contributions of each removal pathway to the total super-droplet count loss in each 1-s interval. Panels (e,f) show the time series of domain-mean turbulent kinetic energy (TKE). This diagnostic is based on super-droplet count loss, not liquid-water mass loss.

Comparison with K-CPEC expansion experiments

To assess whether the babyEULAG SDM configuration used in this study produces realistic cloud evolution in an expansion chamber, we compare it with expansion experiments performed in the Korea Cloud Physics Experimental Chamber (K-CPEC; Park et al., 2025). K-CPEC is a 3 m×3 m×3 m cloud chamber that is cooled from an initial temperature of about -10 °C with an effective ascent rate of 5 m s^{-1}. In the experiment, cloud development is monitored with a Welas optical particle counter that records the time evolution of the droplet size distribution and of droplet number concentrations for selected diameter thresholds.

For the comparison shown in Fig. S2, we run babyEULAG–SDM in a 3 m × 3 m × 3 m domain initialized to the K-CPEC conditions ($T = -10$ °C; nominal ascent rate 5 m s^{-1}). The simulation follows the idealized homogeneous cooling procedure described in Sect. 2, in which temperature and pressure are reduced uniformly in all grid cells and the wall temperature is relaxed toward the chamber mean to minimize net heat fluxes. This differs from the real K-CPEC expansion, where air is removed locally by a vacuum pump and wall temperatures can evolve differently from the interior; therefore, the detailed time evolution of thermodynamic variables is not expected to match exactly. To keep the number of super-droplets computationally tractable in the larger K-CPEC volume, the grid spacing is doubled relative to our standard KIST setup ($\Delta x = \Delta y = 0.08$ m; $\Delta z = 0.04$ m).

Ice-nucleating particles are represented by an externally mixed Arizona Test Dust (ATD) population. The ATD dry number size distribution is taken from the AIDA experiments of Möhler et al. (2006), described by a lognormal distribution with a median diameter of 0.35 μm and a geometric standard deviation of 1.65. Water uptake and activation of ATD particles are parameterized using the Frenkel–Halsey–Hill (FHH) adsorption activation framework (Kumar et al., 2011) with $A_{FHH} = 2.96$ and $B_{FHH} = 1.28$. Heterogeneous freezing is parameterized using the INAS formulation of Niemand et al. (2012), and the total ATD number concentration is set to 1000 cm^{-3}.

Figure S2a shows the simulated time evolution of the domain-mean droplet size distribution dN/dlog D. After an initial activation burst around 1–2 minutes, droplets rapidly grow into the 10–20 μm range, and later in the run the number of droplets near 10 μm decreases while the size distribution shifts toward diameters of order 100 μm, with droplets around 100 μm becoming most abundant. This behaviour closely resembles the Welas OPC spectra reported for the corresponding K-CPEC expansion experiment. Figure S2b shows the simulated number concentrations of droplets with diameters $D \geq 2$ μm and $D \geq 20$ μm. The concentration of droplets with $D \geq 2$ μm quickly rises to values close to 10 cm^{-3}, while droplets with $D \geq 20$ μm increase more gradually and reach peak values of order 10 cm^{-3}. These magnitudes and temporal evolutions are comparable to the observed values in Park et al. (2025).

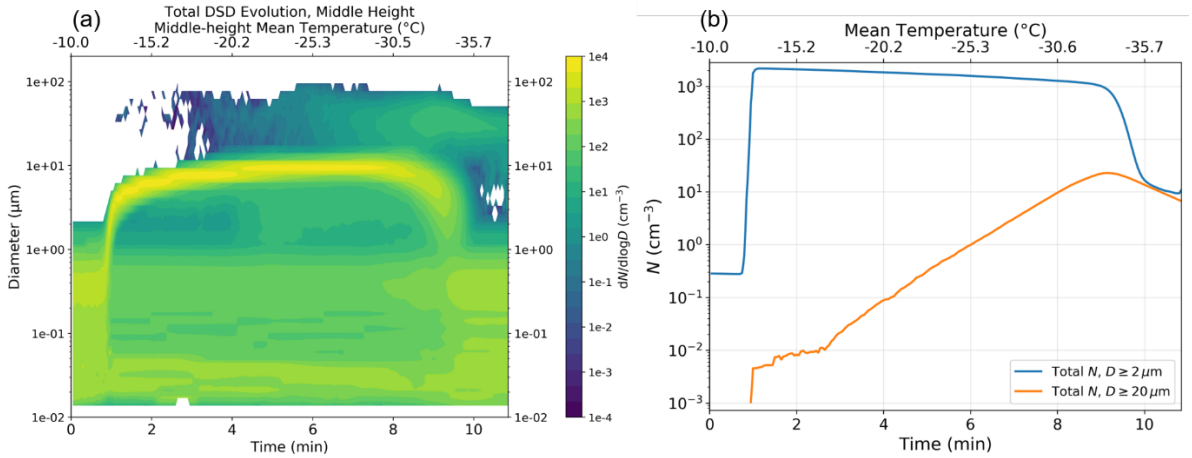


Figure S2. babyEULAG SDM simulation configured to mimic the K-CPEC expansion experiment of Park et al. (2025) with an initial temperature of -10 °C and an effective ascent rate of 5 m s^{-1} in a 3 m×3 m×3 m chamber. Panel (a) shows the time evolution of the domain-mean size distribution of all cloud particles (liquid droplets and ice crystals), expressed as dN/dlog$D$. Panel (b) shows the number concentration of droplets with diameters D≥2 μm and D≥20 μm as a function of time.

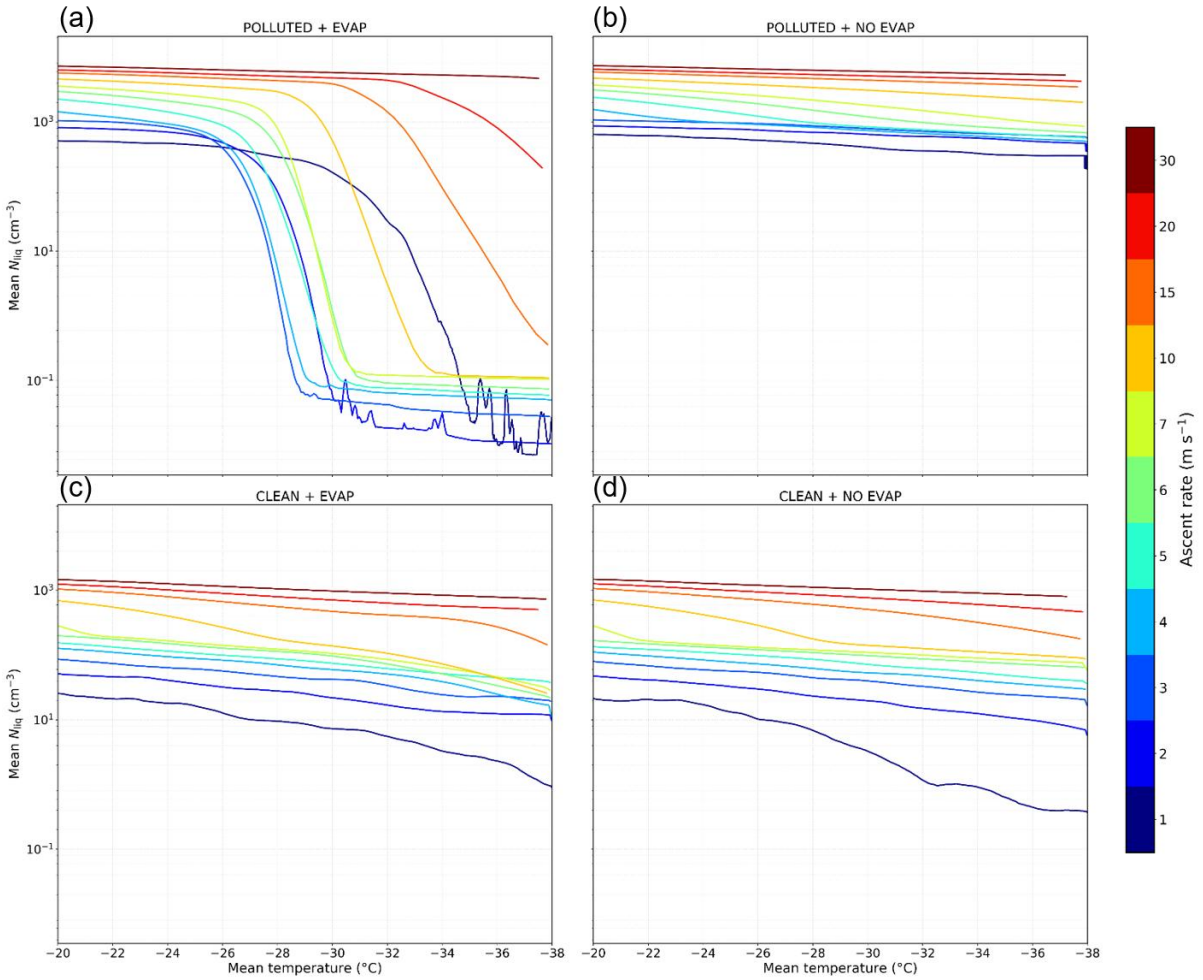


Figure S3. The domain-mean liquid droplet number concentration N_{liq} (for droplets with r_{liq}>1 μm) as a function of mean cloud chamber temperature for all sensitivity experiments. The top row shows the polluted Seoul case and the bottom row shows the N_{sol}-reduced (clean) case. The left column corresponds to simulations with liquid droplet evaporation (EVAP) and the right column to simulations without evaporation (NOEVAP). Line color indicates the imposed ascent rate from 1 to 30 m s^{-1}. The vertical axis is shown on a logarithmic scale.

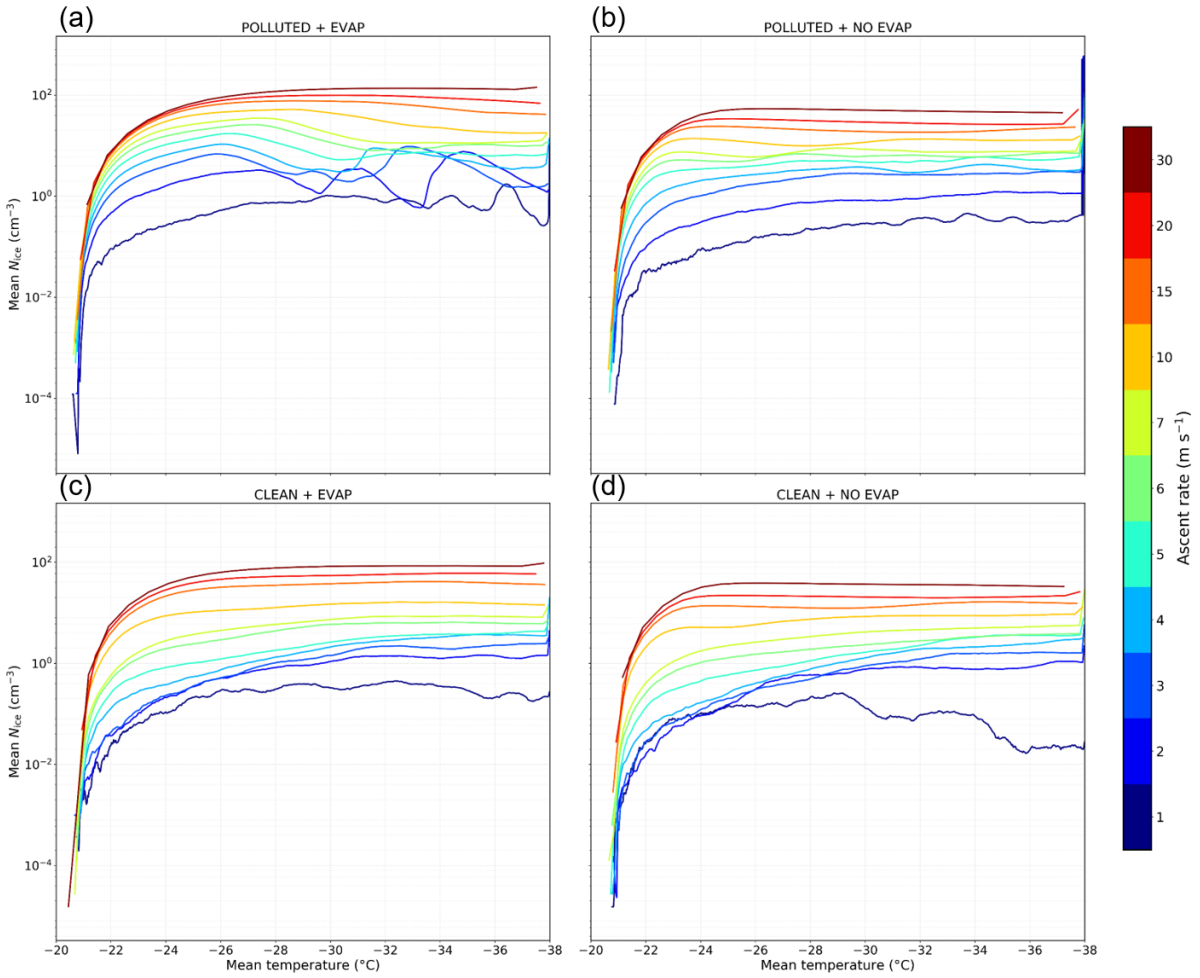


Figure S4. Same as Figure S3, except for domain-mean ice crystal number concentration N_{ice} (for ice crystal with r_{ice}>1 μm) as a function of mean cloud chamber temperature for all sensitivity experiments.

Supersaturation fields relative to ice

Figure S5 presents the corresponding domain-mean supersaturation with respect to ice, S_{ice}. The dotted line denotes the value of S_{ice} corresponding to saturation with respect to liquid water ($S_{liq} = 0$). Values of S_{ice} between zero and this reference indicate vapor pressures between ice and liquid-water saturation and therefore thermodynamic conditions favorable for WBF. In the polluted EVAP simulations, S_{ice} remains positive and frequently falls below the liquid-saturation reference after ice formation, consistent with the negative S_{liq} shown in Fig. 8. The NOEVAP simulations generally remain closer to the liquid-saturation reference. This separation from the reference indicates that the chamber air becomes strongly subsaturated with respect to liquid while staying supersaturated with respect to ice, so conditions favor vapor transfer from evaporating droplets to growing ice through WBF-related deposition. The elevated S_{ice} in EVAP is sustained because droplet evaporation continuously supplies additional water vapor under liquid subsaturation, which can then be taken up by ice through vapor deposition. In the NOEVAP counterparts, this vapor source is absent, so S_{ice} stays closer to the saturation-over-liquid reference and decreases earlier as depositional growth draws down the available supersaturation.

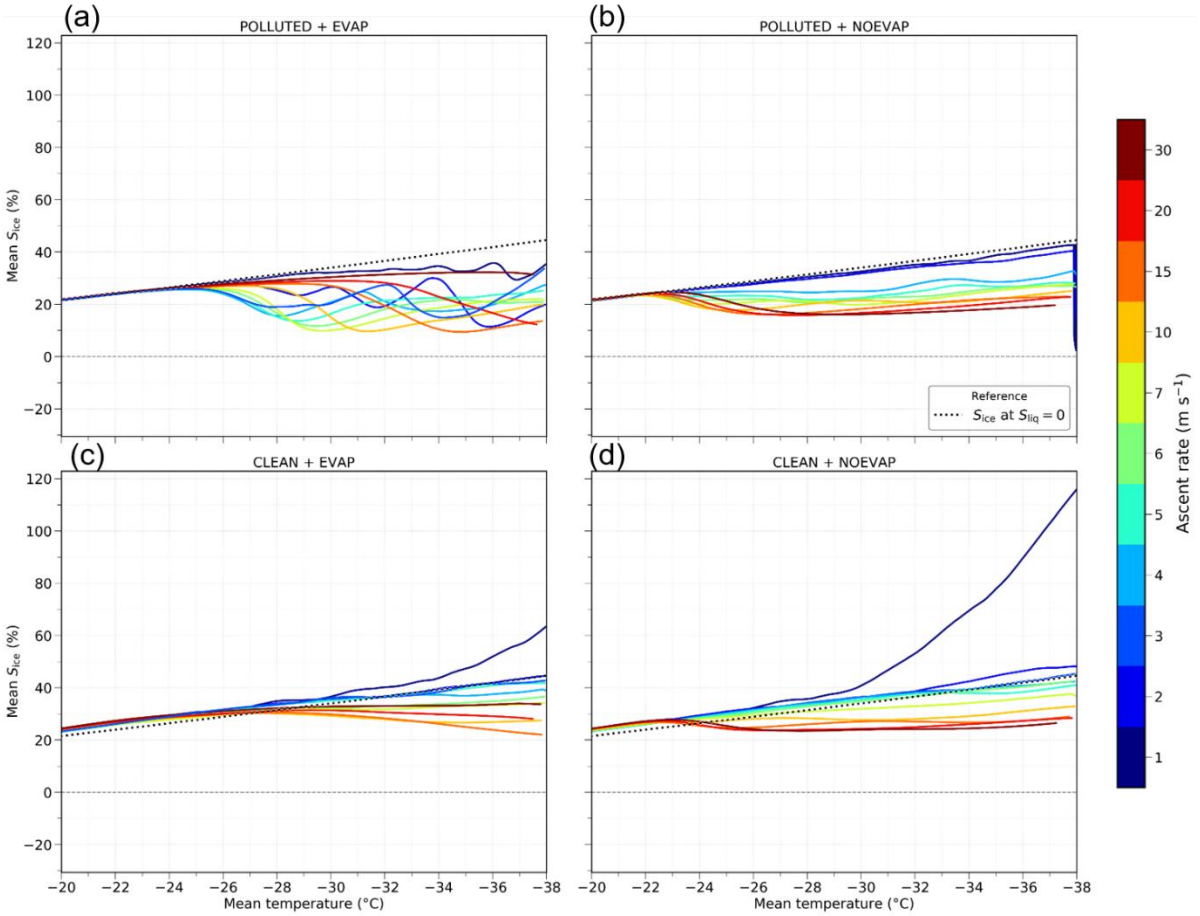


Figure S5. Same as Figure S3, except that the vertical axis shows the domain-mean supersaturation with respect to ice, S_{ice}. The dotted line indicates the value of S_{ice} that corresponds to saturation with respect to liquid water (S_{liq}=0).

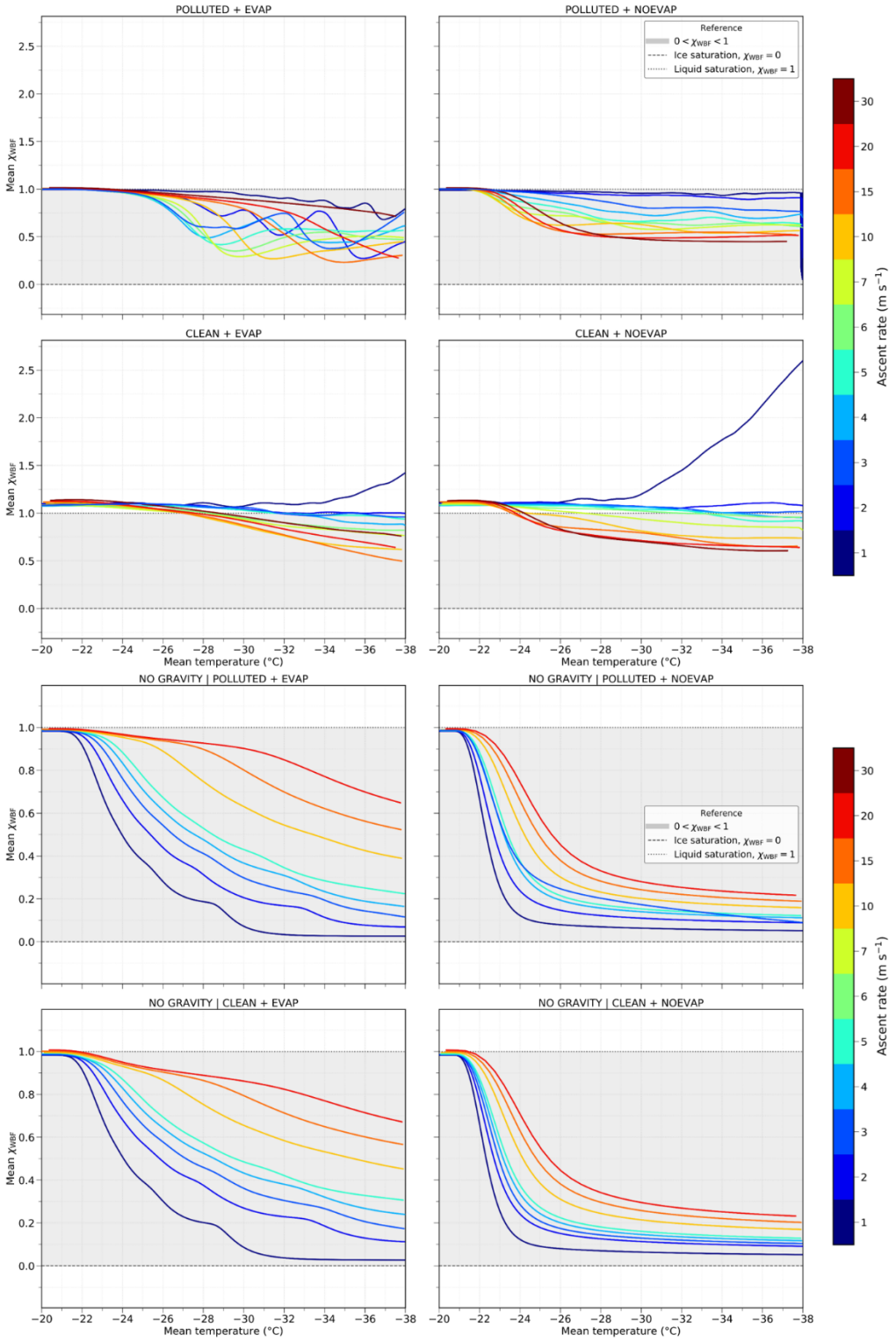


Figure S6. Domain-mean thermodynamic WBF-regime parameter, $\chi_{WBF} = (e - e_{s,i})/(e_{s,w} - e_{s,i})$, as a function of mean cloud-chamber temperature. The left and right columns show the EVAP and NOEVAP simulations, respectively. The upper two rows show the gravity-on simulations, and the lower two rows show the corresponding no-gravity simulations. Within each pair of rows, the upper row shows the polluted Seoul aerosol cases and the lower row shows the clean cases with N_{sol} reduced by a factor of 10. Line color indicates the imposed ascent rate from 1 to 30 m s^{-1}. The gray shading indicates $0 < \chi_{WBF} < 1$, corresponding to vapor pressures between ice and liquid-water saturation and therefore thermodynamic conditions favorable for WBF. The dashed and dotted horizontal lines indicate ice saturation ($\chi_{WBF} = 0$) and liquid-water saturation ($\chi_{WBF} = 1$), respectively.

Interpreting the non-monotonic ascent-rate dependence of r_p/r_e in the no-gravity EVAP simulations

Figures S7–S9 provide supporting diagnostics to explain why the ice aspect ratio (r_p/r_e) shows a non-monotonic dependence on ascent rate in some no-gravity EVAP simulations, and why this behavior changes as INP loading decreases. Figure S7 shows the domain-mean supersaturation with respect to ice, S_{ice}, as a function of mean cloud chamber temperature for three INP number concentration (N_{INP}) settings: the reference case used in the main text (N_{INP}=1500 cm^{-3}; Fig. S7a), a reduced-N_{INP} sensitivity (N_{INP}=500 cm^{-3}; Fig. S7b), and a very-low-N_{INP} sensitivity (N_{INP}=50 cm^{-3}; Fig. S7c). Figure S8 shows the corresponding domain-mean normalized WBF intensity metric u_z^* (U_z^*/w) for the same three INP settings (Fig. S8a–c). Finally, Figure S9 shows the resulting habit ratio r_p/r_e for the 500 and 50 cm^{-3} cases (Fig. S9a and Fig. S9b, respectively).

The central idea is that habit evolution requires time spent in a regime of active depositional growth. Slow ascent rate generally increases residence time in the mixed-phase temperature range, which should favor anisotropic growth and larger r_p/r_e. However, when WBF is very strong, depositional growth can rapidly consume ice supersaturation and deplete the vapor reservoir. In that case, deposition becomes supply-limited early, and the period of sustained depositional growth is shortened. This creates a tradeoff: slow ascent rate provides time, but it can also intensify WBF enough to shut off S_{ice} too early, limiting the accumulation of habit anisotropy.

This tradeoff is evident in the higher-N_{INP} simulations. In the reference case (N_{INP} = 1500 cm^{-3}), u_z^* can reach very large peak values early in the mixed-phase stage (Fig. S8a). When maximum u_z^* becomes very large (a useful indicator is maximum $u_z^* \gtrsim 8$), S_{ice} drops sharply afterward (Fig. S7a), consistent with rapid vapor depletion by intense WBF-driven deposition. Once S_{ice} collapses, continued deposition is strongly limited, so r_p/r_e cannot keep increasing efficiently even though the cloud remains within mixed-phase temperatures. As a result, the largest habit signal does not necessarily occur at the slowest ascent rate. Instead, an intermediate ascent rate can produce the largest r_p/r_e because it delays severe vapor depletion while still providing substantial time for depositional growth. This is consistent with the main-text behavior where the peak r_p/r_e for the higher-N_{INP} cases occurs at an intermediate ascent rate (see Fig. 14).

When N_{INP} is reduced to 500 cm^{-3}, the total depositional sink is weaker. Consistent with that, S_{ice} remains elevated for longer at a given ascent rate (Fig. S7b), and the peak u_z^* is generally reduced and less prone to reaching extremely large values (Fig. S8b). Because vapor depletion occurs later (or is less severe), the system can sustain active depositional growth for a longer fraction of the mixed-phase stage. In this regime, slower ascent rate becomes more favorable, and the ascent rate that maximizes r_p/r_e shifts toward slower values, while the attainable maximum increases (Fig. S9a and also Fig. 14). Physically, lowering INP reduces the strength of WBF enough that the benefit of longer residence time is no longer offset as strongly by early depletion of S_{ice}.

The very-low-N_{INP} simulations (N_{INP} = 50 cm^{-3}) show an even clearer limiting regime. Here WBF is substantially weaker, u_z^* remains comparatively modest across ascent rates (Fig. S8c), and S_{ice} does not exhibit the rapid early collapse seen at higher INP loadings (Fig. S7c). In the absence of strong vapor-exhaustion events, the ascent-rate dependence of habit becomes monotonic and controlled primarily by available time for depositional growth. Accordingly, the slowest ascent rate (1 m s^{-1}) produces the largest habit ratio, reaching $r_p/r_e \approx 3.7$, and r_p/r_e decreases monotonically as ascent rate increases (Fig. S9b). This monotonic decrease reflects a simple residence-time control: faster ascent rate shortens the mixed-phase growth window, leaving less time for anisotropic depositional growth to accumulate.

In summary, Figures S7–S9 support an interpretation in which the ascent-rate dependence of r_p/r_e is governed by the duration of active depositional growth. Slow ascent rate increases residence time, but at sufficiently high N_{INP} it can also produce very intense WBF (large peak u_z^*) that rapidly depletes S_{ice} and terminates sustained deposition early. Faster ascent rate avoids early depletion but reduces the time available for habit evolution. This competition yields a peak r_p/r_e at an intermediate ascent rate when N_{INP} is high enough for vapor depletion to matter, while at very low N_{INP} the dependence becomes monotonic because vapor depletion is weak and residence time dominates.

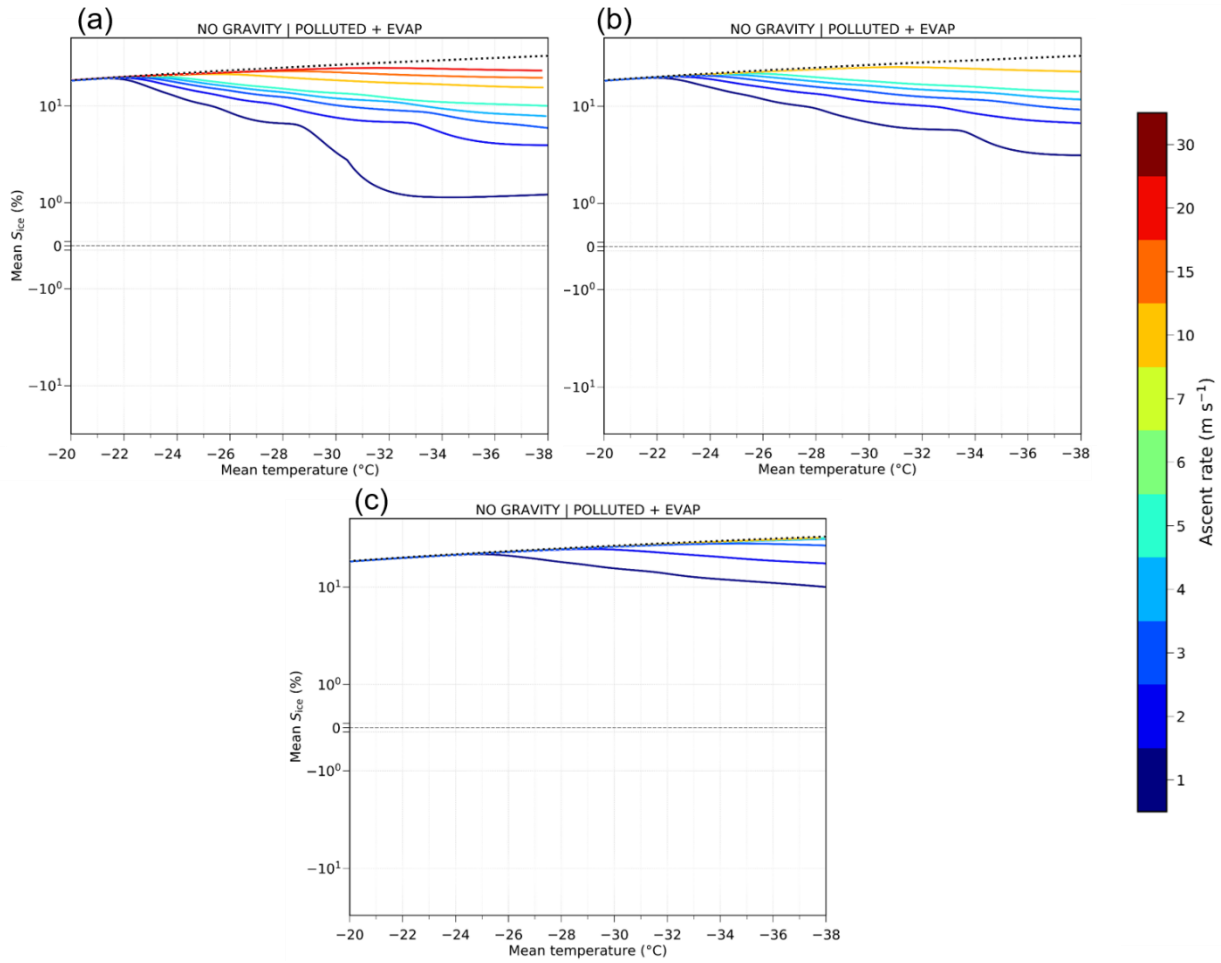


Figure S7. Domain-mean supersaturation with respect to ice, S_{ice}, as a function of mean cloud chamber temperature for the no gravity simulations. Panel (a) shows the reference case used in the main text (INP number concentration N_{INP} = 1500 cm^{-3}). Panel (b) shows the reduced-INP sensitivity cases (N_{INP} = 500 cm^{-3}). Panel (c) shows the very-low-INP sensitivity cases (N_{INP} = 50 cm^{-3}). The dotted line indicates the value of S_{ice} that corresponds to saturation with respect to liquid water (S_{liq}=0). Line color indicates the imposed ascent rate from 1 to 10 m s^{-1}

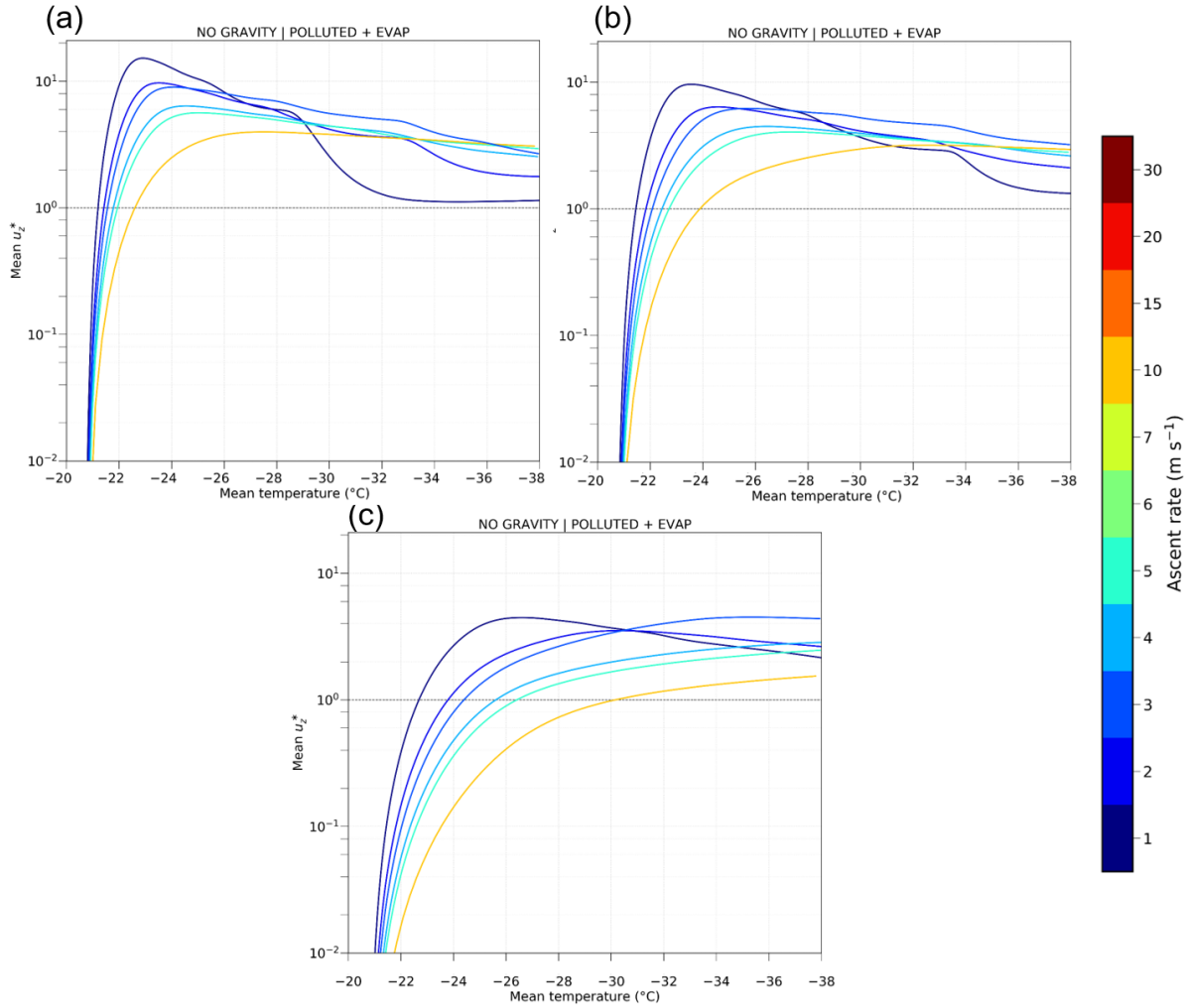


Figure S8. Same as Figure S7, except that the vertical axis shows the domain-mean u_z^*.

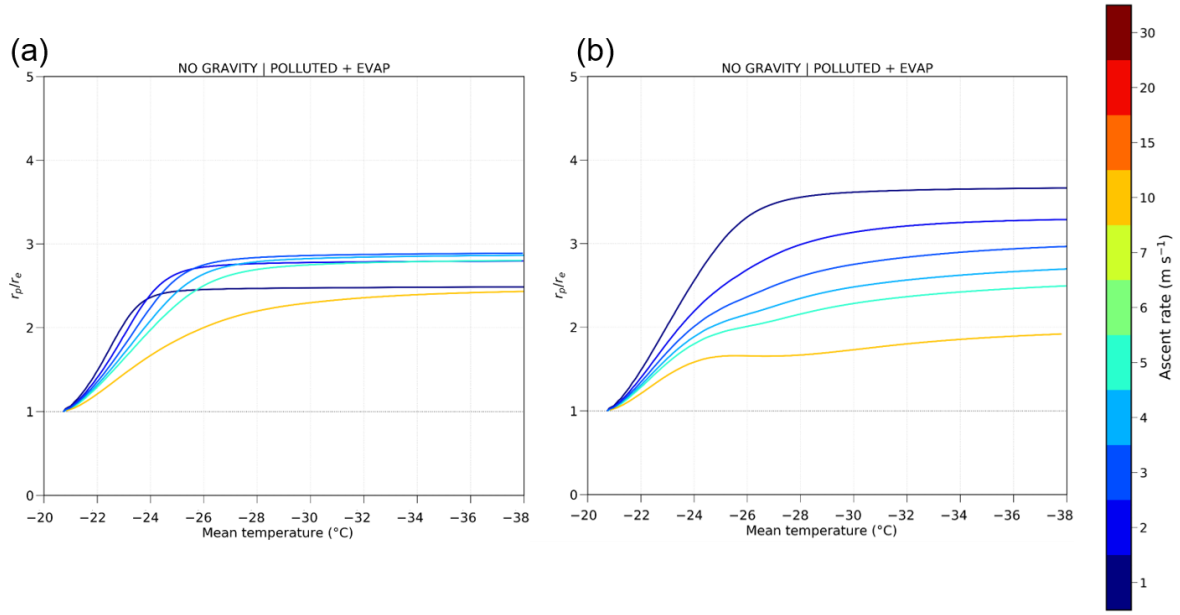


Figure S9. Mean polar (r_p) to equatorial radius (r_e) ratio r_p/r_e as a function of mean cloud chamber temperature for the no gravity simulations. Panel (a) shows the reduced-INP sensitivity cases (INP number concentration = 500 cm^{-3}). Panel (b) shows the very-low-INP sensitivity cases (INP number concentration =50 cm^{-3}). Line color indicates the imposed ascent rate from 1 to 10 m s^{-1}

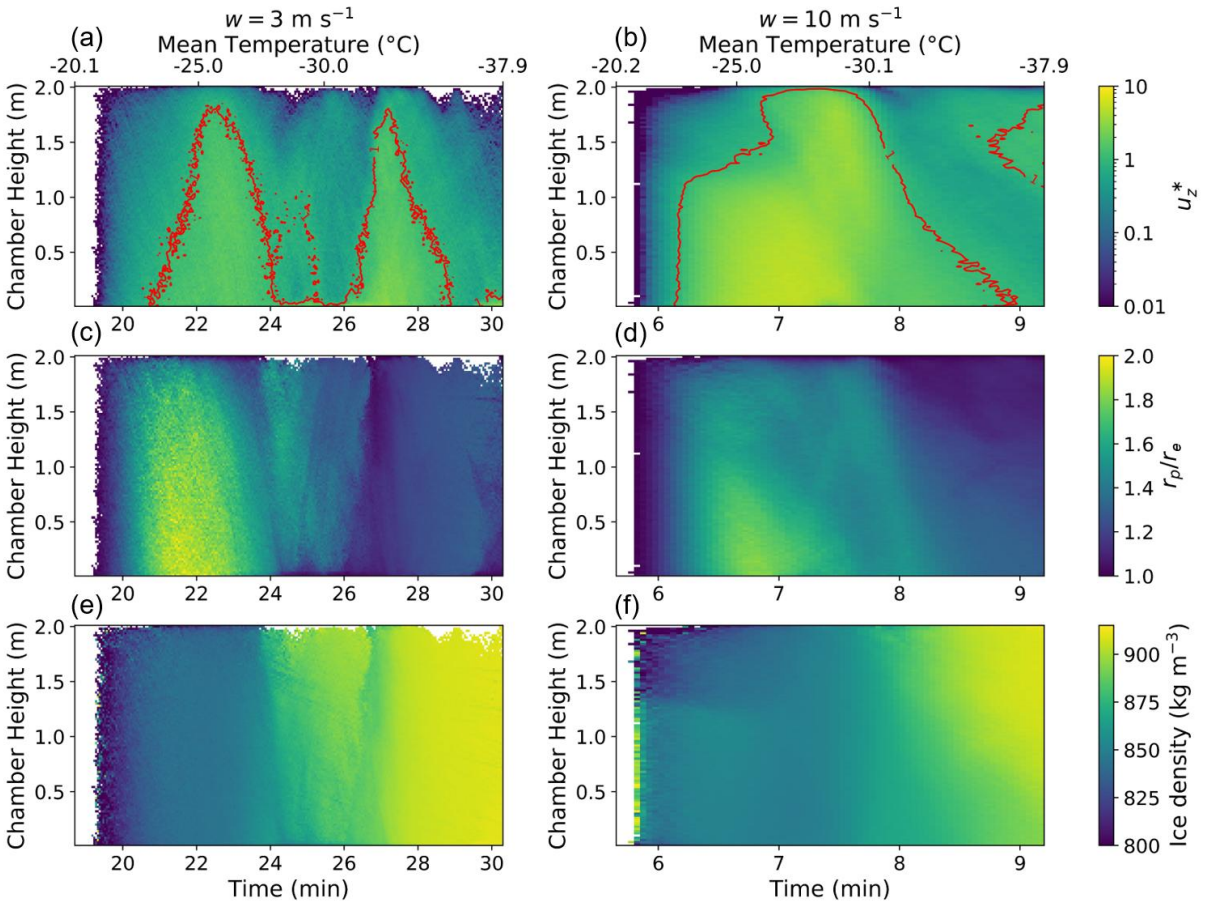


Figure S10. Time–height evolution of u_z^*, crystal aspect ratio, and apparent ice density for the polluted Seoul EVAP simulations with gravity. Panels (a), (c), and (e) show the experiment with an imposed ascent rate of w=3 m s^{-1}, and panels (b), (d), and (f) show the experiment with w=10 m s^{-1}. The top row gives u_z^* (color shading), with the red contour indicating u_z^*=1. The middle row shows the mean aspect ratio r_p/r_e, and the bottom row shows the mean apparent ice density. The x-axis indicates time since the start of expansion, and the upper axis in each top panel shows the corresponding mean cloud chamber temperature. Only the mixed-phase temperature range between about −20 and -38 °C is shown.

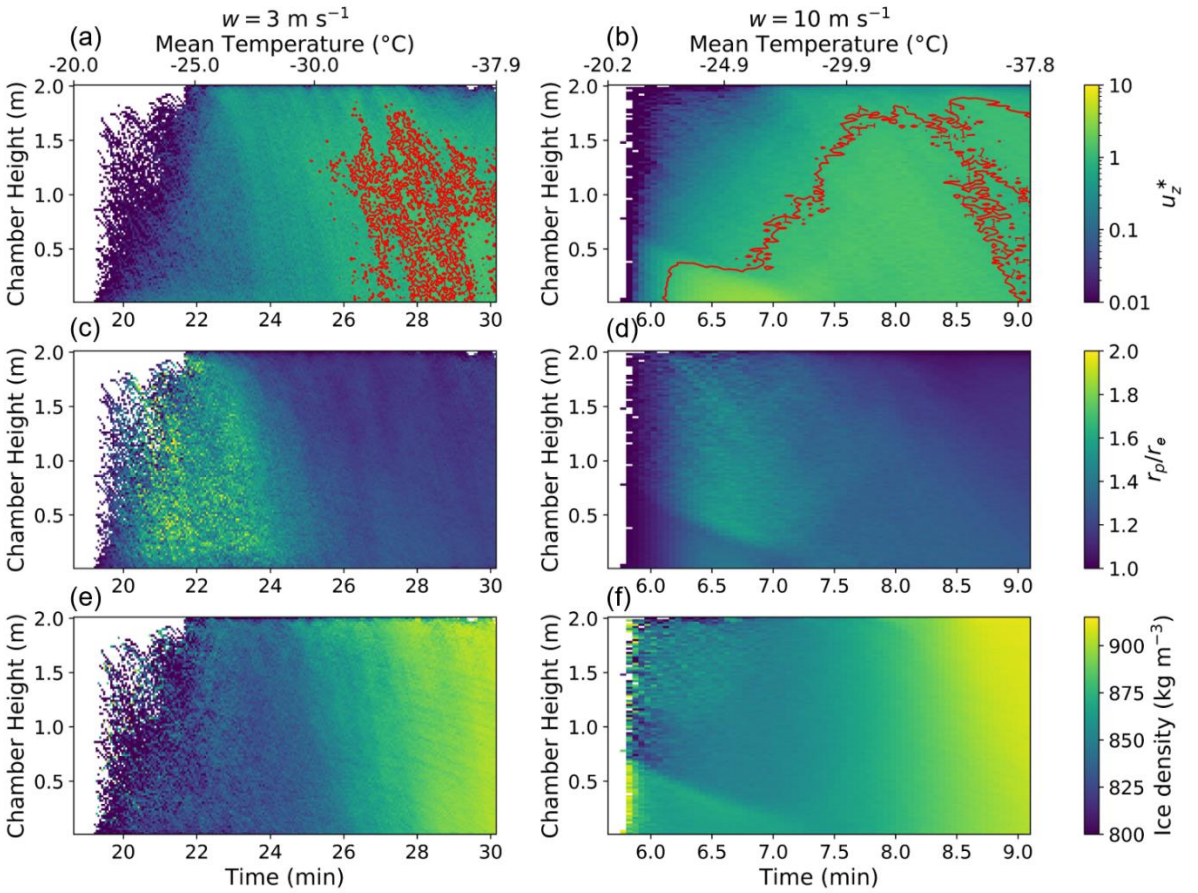


Figure S11. Same as Figure S10, but for the N_{sol}-reduced clean aerosol case.

References

Niemand, M., Möhler, O., Vogel, B., Vogel, H., Hoose, C., Connolly, P., Klein, H., Bingemer, H., DeMott, P. J., Skrotzki, J., and Leisner, T.: A particle-surface-area-based parameterization of immersion freezing on desert dust particles, J. Atmos. Sci., 69, 3077–3092, https://doi.org/10.1175/JAS-D-11-0249.1, 2012.